Pol. J. Environ. Stud. Vol. 34, No. 1 (2025), 213-225
DOI: *10.15244/pjoes/183565* ONLINE PUBLICATION DATE: 2024-07-25

Original Research

Adsorption of Reactive Blue 13 from Dyeing Wastewater onto Mesoporous Carbon Xerogels

Huiyun Lu, Jianjiong Zhu, Donglei Li, Jiahang Liu, Rui Yao, Min Yao*

School of Civil & Environmental Engineering and Geography Science, Ningbo University, Ningbo 315211, China

Received: 6 December 2023
Accepted: 31 January 2024

Abstract

Carbon xerogel is a nano-scale adsorption material with abundant mesopores and large adsorption capacity. A series of mesoporous carbon xerogels (MCX) were synthesized in the process of polycondensation of resorcinol and formaldehyde using different resorcinol/sodium carbonate catalyst molar ratios (R/C = 100~3000). And the adsorption behavior of the MCX for the azo dye reactive blue 13 (RB13) from dyeing wastewater was investigated in this study. Results showed that variations in both specific surface area and pore size distribution of MCX were closely related to the amount of catalyst. The MCX exhibited maximal surface area, abundant mesoporosity, and highest adsorption capacity for RB13 when the molar ratio of R/C was 1000. The adsorption of RB13 by MCX1000 proceeded rapidly in the first 50 min and reached equilibrium in 180 min. The adsorption process was exothermic, spontaneous, and can be well fitted by the pseudo-second-order and Temkin models, with the maximum sorption capacity of 184.36 $mg \cdot g^{-1}$. The adsorption of RB13 onto MCX was attributed to physicochemical adsorption. The main adsorption mechanisms of the MCX for RB13 were the electrostatic interaction, hydrogen bonding and van der Waals forces between dye molecules and functional groups, such as -OH, and -C-O, etc.

Keywords: Mesoporous carbon xerogels, Reactive Blue 13, adsorption

Introduction

Organic dyes are the crucial components of the fine chemical industry, with extensive application in various fields, such as fabric, plastic, leather, paint, paper manufacturing, and the food and beverage industries [1-3]. However, the production and utilization of these compounds result in a large amount of colored wastewater. Considering their high solubility in water, it is expected that around 10%～20% of the dyes will be lost in the wastewater during the manufacturing process, with almost 50% entering the wastewater flows during coloring and other related procedures [4-6]. It has been reported that specific azo dyes, particularly an extensive array of reactive dyes and their resulting byproducts, have been demonstrated to exert detrimental impacts on human well-being [7]. These effects encompass eliciting hyperimmune responses, inducing cellular damage and inflammatory reactions, and potentially instigating carcinogenesis subsequent to human exposure [8-10]. Thus, their removal from the wastewater before being discharged into the environment is of great importance. Among the extensively employed techniques for achieving this objective are coagulation, flotation,

*e-mail: yaomin@nbu.edu.cn;
Tel. +86-135-8683-1947

adsorption, advanced oxidation, microbial degradation, membrane separation, and similar approaches [11-18]. The adsorption process is considered as a relatively efficient method for the removal of dyes and other organic pollutants [19].

Various kinds of adsorbent materials have been employed to eliminate dyes from wastewater, such as activated carbon, carbon nanotubes, Graphene-based materials, and so on [20-24]. Notably, carbon xerogels, an emerging porous nanomaterial hitherto developed over the past three decades, have gained significant popularity and proven to be remarkably efficacious as adsorbents for pollutants present in the liquid phase [25-27]. Magdalena et al. studied the adsorption of anionic dyes by carbon xerogels, which showed that the adsorption capacity ranged from 83 to 140 $mg \cdot g^{-1}$, higher than conventional activated carbon [28]. Some studies have shown that the adsorption of methyl red and rhodamine dyes on carbon xerogel is significantly better than that of carbon nanotubes functionalized with -COOH [29, 30]. Other studies have shown that carbon xerogel has a better adsorption effect on EBT dyes than biochar [31, 32]. Furthermore, in order to further improve the adsorption capacity for macromolecular pollutants, we can also use the advantage of adjustable pore size of carbon xerogel to prepare mesoporous carbon xerogel (MCX) with rich mesopores by adjusting the proportion of raw materials and reaction parameters during the synthesis process.

In this study, the preparation of a sequence of MCX with varying pore sizes and the adsorption mechanism of Reactive blue 13 (abbreviated as RB13) were evaluated. The primary purposes of this study were varied: (i) to ascertain the optimal ratio of raw materials for the synthesis of MCX; (ii) to analyze the relationship between adsorbent dosage and its effects, contact time, contaminant concentrations, and adsorption temperature on the adsorption process pertaining to RB13; (iii) to reveal the underlying adsorption mechanism through analysis encompassing adsorption isotherm and kinetic models; and (iv) to further elucidate the correlation between structure and adsorption capability via a comparative assessment of pore structure, surface topography, and functional groups of MCX before and after adsorbing.

Experimental

Chemicals and Materials

All utilized chemicals were of analytical purity without any purification, and deionized water was used throughout the experiments. Resorcinol, formaldehyde aqueous solution (40 wt. %), sodium carbonate and acetone were supplied by Shanghai Hushi Laboratory Equipment Co. LTD. RB13 was purchased from Aladdin (Shanghai) Reagent Co. LTD. Its chemical structure was shown in Fig. 1.

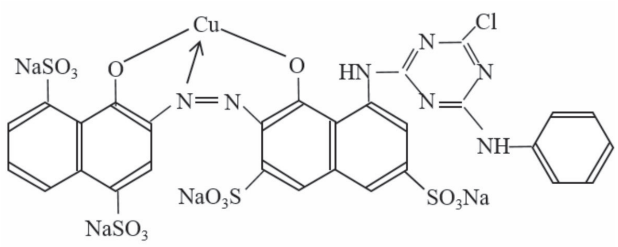

Fig. 1. Chemical structure of RB13.

Preparation of Mesoporous Carbon Xerogels

The organic gels were synthesized according to the method of Pekala (Fig. 2) [25]. 11 g of resorcinol (R) and different doses of sodium carbonate as the catalyst (C) were dissolved in 10 ml of deionized water by stirring at 600 rpm for 30 minutes at room temperature. After homogenizing with 15 g formaldehyde aqueous solution (F), the solution was stirred for 60 minutes and poured into glass tubes (i.d. 6 mm, length ca. 10 cm), which were then sealed by parafilm and cured successively in the drying oven at 298 K for 1 day, 323 K for 1 day and 353 K for 5 days. Over the above one-week aging, the dark red hydrogels were formed. Here several molar ratios of resorcinol to catalyst (R/C) were set at 100, 250, 500, 1000, 1500, 2000 and 3000 in order to obtain the optimal mesoporous size of carbon gels. The constant molar ratio of resorcinol to formaldehyde (R/F) of 0.5 was maintained throughout the synthesis. Owing to the undesirability of water for the drying process, the diluent water in the pores was replaced by acetone. Specifically, the aged gel rods were taken out of the glass tubes and immersed into acetone solution, and then extracted for 10 minutes by ultrasonic method three times, renewed with fresh acetone every time. After solvent exchange step, the gels were carbonized in a tube furnace (OTF-1200X, Hefei) under a high purity nitrogen atmosphere (99.996%) where the nitrogen flow was 25 $mL \cdot min^{-1}$. The carbonization program consisted of increasing the heat to 383 K at a rate of heating of 0.5 $K \cdot min^{-1}$, keeping for 5 h and then heating to 1173 K with a heating rate of 5 $K \cdot min^{-1}$, maintaining for 3 h. The carbon xerogels samples were finally ground to 0.074 mm size. Accordingly, a series of mesoporous carbon xerogels (abbreviated as MCX) were obtained for use, which were notated successively as MCX100, MCX250, MCX500, MCX1000, MCX1500, MCX2000 and MCX3000 (the number indicated the R/C molar ratio in the recipe, and as the number increased, the amount of catalyst added decreased). Schematic representation of prepared MCX was shown in Fig. 2.

Characterization and Analysis of Mesoporous Carbon Xerogels

The surface area and porosity of the MCX samples were determined via N_2 adsorption/desorption isotherms

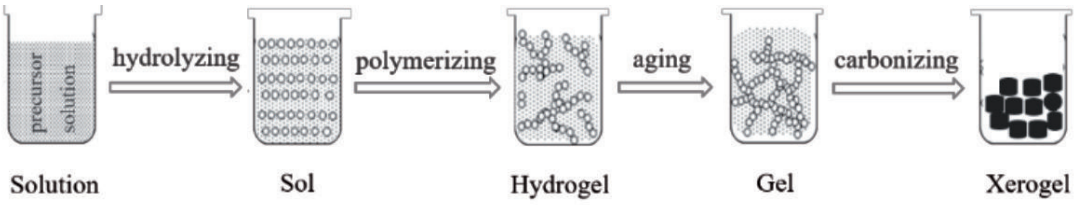

Fig. 2. Synthesis procedure of MCX.

with an Automatic Surface Area & Porosimetry Apparatus (ASAP 2020, Micromeritics, USA). The surface areas (S_{BET}), mesopore volume (V_{meso}) and pore diameter (D_{pore}) were calculated using Brunauer-Emmett-Teller (BET) equation ($p/p_0 < 0.3$), t-plot method ($p/p_0 = 0.99$) and Barrett-Joyner-Halenda (BJH) pore size distribution model ($p/p_0 = 0.2$-0.5), respectively.

Surface morphologies of MCX were examined by the Scanning Electron Microscopy (SEM) (TM-3000, Hitachi, Japan). The samples were attached to the sample holder using adhesive carbon tape and sprayed with Au against charging, and then tested at 100,000 times magnification in a high vacuum mode.

The structure and functional groups of MCX were characterized by Fourier Transform InfraRed Spectrometer (FT-IR) (Nicolet IS10, Bruker, Germany). The FT-IR spectrum was obtained under the condition of 400~4000 cm^{-1} of scan range, 4.0 cm^{-1} of resolution and scanning 32 times.

Adsorption Experiments

In the laboratory, batch adsorption experiments were performed by mixing a 50 mL solution of RB13 with the MCX samples at 180 rpm and 298 K for 12 hours to achieve apparent equilibrium. Afterwards, the mixture was separated by filtering with a 0.45 μm syringe filter, the residual dye concentrations in the filtrate were measured using a UV-VIS Spectrophotometer (U-3900, Hitachi, Japan). The measurements were taken at the wavelength of maximum absorbance of RB13 (λ_{max} = 596 nm). Subsequently, the RB13 adsorption capacity on the MCX samples was determined by calculating Eq. (1):

$$q_e = \frac{(C_0 - C_e)V}{m} \quad (1)$$

Where q_e ($mg \cdot g^{-1}$) represents the equilibrium adsorption capacity of the dye per unit weight of the adsorbent, C_0 and C_e ($mg \cdot g^{-1}$) are the initial and equilibrium concentrations of RB13 in solution, V (L) is the volume of solution, and m (g) is the mass of a given MCX adsorbent.

The effect of adsorbent dosage, initial dye concentration, temperature and contact time on the adsorption of RB13 on MCX were tested, and the isotherms, thermodynamics and kinetics of the adsorption process were obtained accordingly. The pH of the RB13 solution used in the experiment was about 6.8-7.0, which was within the pH range of the actual dyeing wastewater, so no further adjustment was made.

Data Analyzing Method and Model Evaluation

In this study, the software of Excel 2016 (Microsoft Office, USA) and Origin 9.1 (Origin Lab Corporation, USA) were used for the data analysis and statistics. Meanwhile, several mathematical models (Table 1) were selected to fit the data collected from the RB13 adsorption onto the MCX1000 experiment. Because of the inherent bias created by linearization of adsorption models, the nonlinear models have been used here.

The kinetics of pollutants adsorption onto adsorbents holds vital significance in the selection of optimal testing conditions for the adsorption process with the batch technique. The kinetic parameters, crucial for predicting the rate of adsorption, furnish valuable information for the design and modeling of adsorption processes. In this investigation, the kinetics of RB13 adsorption onto MCX1000 were scrutinized employing pseudo-first order, pseudo-second order, intra-particle diffusion, and Elovich models.

The adsorption isotherm, delineating the state of equilibrium between the adsorbent and the adsorbate at a specific temperature, functions as a significant instrument in comprehending the adsorbent's adsorption performance and mechanism. Moreover, it facilitates the assessment of whether the adsorption process conforms to a specific adsorption model. To determine the most suitable isotherm and validate the adsorption mechanism, the data were analyzed considering Freundlich, Langmuir, Temkin, Dubinin-Radushkevich, Redlich-Peterson and Koble-Corrigan isotherm equations.

Adsorption thermodynamics unveils the energy conversions and thermal equilibrium that underlie the adsorption process through the characterization of adsorption enthalpy (ΔH°), adsorption entropy (ΔS°), and adsorption free energy(ΔG°). This enables the evaluation of the reversibility of adsorption reactions and the influence of thermal effects on reaction rates.

Table 1. Kinetic, isotherm and thermodynamic equations used in this study.

Characteristics	Values	Characteristics	Values
Kinetic models		q_t (mg·g^{-1}) : the adsorption amounts at time t; q_e (mg·g^{-1}) : the adsorption amounts at equilibrium; k_1 (min^{-1}): pseudo-first-order rate constant; k_2(g·mg^{-1}·min^{-1}): pseudo-second-order rate constant; k_{int}(mg·g^{-1}·min$^{-1/2}$):intraparticle-diffusion rate constant; C (mg·g^{-1}): the boundary layer thickness; α (mg·g^{-1}·min^{-1}): Elovich initial adsorption rate constant; β (g·mg^{-1}): desorption constant;	
Pseudo-first-order	$q_t = q_e(1-e^{k_1 t})$		[39, 40]
Pseudo-second-order	$q_t = \frac{k_2 q_e^2 t}{1+k_2 q_e t}$		[37, 40, 41]
Intraparticle- diffusion	$q_t = k_{int} t^{1/2} + c$		[42]
Elovich	$q_t = \frac{1}{\beta}\ln(1+\alpha\beta t)$		[3, 43, 44]
Isotherm models		C_e (mg·L^{-1}): equilibrium concentration in solution; K_F (mg$^{1-1/n}$ ·L$^{1/n}$· g^{-1}): Freundlich constant; n: heterogeneity factor; q_{max} (mg·g^{-1}) : the maximum adsorption amounts; K_L (g·L^{-1}): Langmuir constant; b_T (J·mol^{-1}): Temkin constant; K_T (L·mg^{-1}): Temkin adsorption potential; R (8.314 J·(mol·K)$^{-1}$): universal gas constant; T (K): temperature; β (mol^2·J^{-2}): D-R constant related to the adsorption energy; ε (J·mol^{-1}): Polanyi potential; E (kJ·mol^{-1}): the average free energy of adsorption; K_R (L·g^{-1}), α_R (L·mg^{-1}): R-P constants; g: R-P isotherm exponent; a_K (L·g^{-1}), b_K (L·mg^{-1}): K-C constants; n: K-C isotherm exponent.	
Freundlich	$q_e = K_F C_e^{1/n}$		[44, 45]
Langmuir	$q_e = \frac{q_{max} K_L C_e}{1+K_L C_e}$		[45]
Temkin	$q_e = \frac{RT}{b_T}\ln(K_T C_e)$		[46, 47]
Dubinin-Radushkevich (D-R)	$q_e = q_{max} e^{\beta\varepsilon^2}$ $\varepsilon = RT\ln(1+\frac{1}{c_e})$ $E = \frac{1}{\sqrt{2\beta}}$		[41]
Redlich-Peterson (R-P)	$q_e = \frac{K_R C_e}{1+á_R C_e^g}$		[38, 39]
Koble-Corrigan (K-C)	$q_e = \frac{\partial_K C_e^n}{1+b_K C_e^n}$		[40, 48]
Thermodynamic equations			
	$\Delta G = -RT\ln K_c$ $\Delta G = \Delta H - T\Delta S$ $K_c = C_s / C_e$	ΔG (kJ·mol^{-1}): Gibbs free energy; ΔH (kJ·mol^{-1}): enthalpy; ΔS (kJ·mol^{-1}): entropy; K_c: the distribution coefficient for adsorption; C_s and C_e (mg·L^{-1}): the adsorbed and equilibrium concentrations.	[9, 38, 40]

Results and Discussion

Characterization of MCX Adsorbents

Characterization of Pore Structure

The structural and textural properties of MCX samples can be determined through detailed characterization. The pore size distribution and pore characterization of MCX samples are shown in Fig. 3 and Table 2, respectively, with varying amounts of catalyst. As evidenced by Fig. 3, the N_2 adsorption/desorption isotherms exhibited the attributes of Type IV isotherms, signifying the presence of mesoporous structures in the prepared sample [32]. Additionally, hysteresis occurred during the capillary condensation phase at relative pressure p/p_0=0.9, indicating the existence of a large sized mesopore in the sample. This result was similar to the adsorption curve obtained by María Canal-Rodríguez's characterization of N-doped carbon xerogels [33]. Notably, among all the prepared samples, MCX1000，which was synthesized at an R/C molar ratio of 1000 had the largest specific surface area of 583.8 m^2·g^{-1}.

Table 2. N_2 adsorption performance parameters.

Samples	S_{BET} ($m^2 \cdot g^{-1}$)	S_{micro} ($m^2 \cdot g^{-1}$)	S_{meso} ($m^2 \cdot g^{-1}$)	V_{meso} ($cm^3 \cdot g^{-1}$)	V_{total} ($cm^3 \cdot g^{-1}$)	d_{pave} (nm)
MCX500	494.8	298.9	195.8	0.23	0.37	2.98
MCX1000	583.8	371.3	197.3	0.54	0.72	4.91
MCX1500	549.4	368.1	162.9	0.63	0.81	5.86
MCX1000 after adsorption	309.5	132.5	177.0	0.46	0.56	7.24

Fig. 4 presented the pore-size distribution analysis of the MCX samples. For MCX1000, the microspores showed an average diameter ranging from 1.7 to 2 nm, while the mesopores have average diameters between 2 and 32 nm. Similarly, for MCX1500, the microspores displayed an average diameter within the range of 1.7-2 nm, whereas the mesopores showed average diameters spanning from 2 to 45 nm. In the case of MCX500, the mesopores presented an average diameter varying from 2 to 12 nm. Notably, the pore-size distribution profiles of these mesoporous carbon xerogels showed a main distribution of 2-45 nm, also indicating that these materials were composed of a large amount of mesopores. The pore size distribution peaks

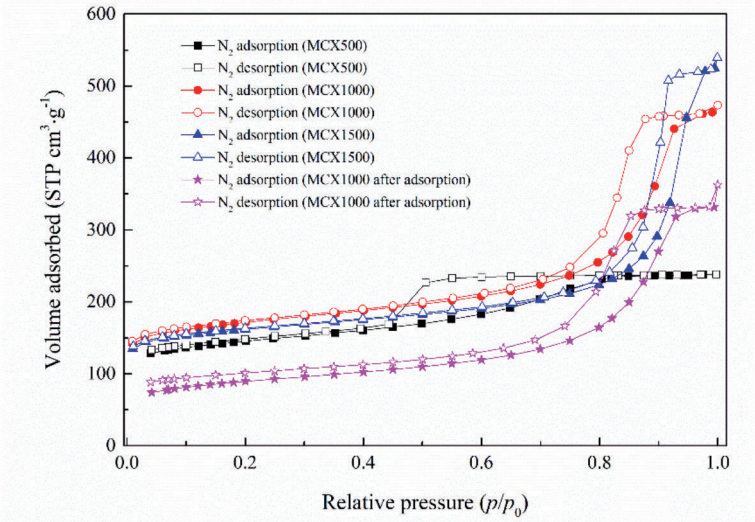

Fig. 3. N_2 adsorption/desorption isotherms of some of the MCX samples.

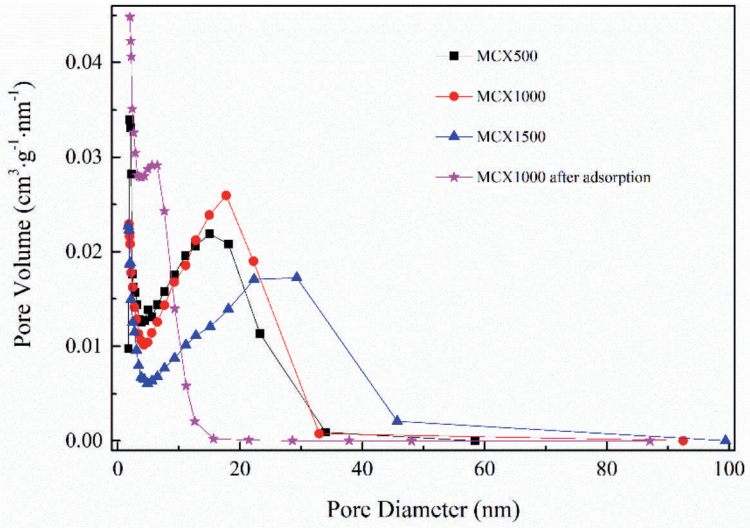

Fig. 4. Pore size distribution of some of the MCX samples.

of the carbon gels experienced a decreasing trend after the adsorption of RB13, while an increased presence of a limited number of micropores. This phenomenon could primarily be attributed to the adsorption of RB13 molecules on the surfaces of mesopores and macropores in the carbon gels, leading to some macropores being blocked. Additionally, as shown in Table 2, there was a notable decline in both specific surface area and pore volume of the adsorbed carbon gel, indicating that RB13 was adsorbed successfully onto the MCX1000.

SEM

SEM images of the samples were presented in Fig. 5. It was noted that the mesoporous carbon xerogels were composed of nano-sized particles with distinct particle sizes as depicted in Fig. 5(a, b, c). Specifically, the size range of MCX500, MCX1000, and MCX1500 was approximately 10 nm, 50 nm, and 100 nm, respectively. Therefore, the size of the mesoporous carbon xerogel particles decreased as the amount of added catalyst increased. The main reason was that the acidity or alkalinity of the initial solution during the preparation would have a certain influence on the properties and surface morphology of the absorbent. With the increase of the amount of sodium carbonate, the pH also rose, which affected the properties of the absorbent surface. Moreover, compared with the morphology of MCX1000, the surface structure after adsorption of MCX1000 was smoother and fuller. Consequently, the uniform adsorption of RB13 onto the surface of MCX1000 was demonstrated.

FT-IR

In order to gain detailed insights into the chemical composition of MCX1000 and verify the successful sorption of RB13 onto it, we conducted FT-IR characterization analysis on the MCX1000 samples as depicted in Fig. 6. The characteristic peaks of MCX1000 could be observed from the black curve. It was established that the stretching vibrations absorption peak of -OH is the broad absorption peak at 3320 cm^{-1}. The -C-O stretching vibrations were responsible for the absorption band at 1060 cm^{-1}.The blue curve revealed that MCX1000 after sorption featured both the old MCX1000 distinctive peaks as well as the new ones. The in plane deformation vibration of C=N caused the absorption peak at 1622 cm^{-1}, which demonstrated a successful sorption of dye onto the MCX1000. Additionally, the vibrational peaks for -OH and -C-O were blue switched towards 3470 cm^{-1} and 1154 cm^{-1}, respectively; the reason was that there was electrostatic attraction between dye molecules and -OH, -C-O and others, functional groups of MCX, hydrogen bond action, and van der Waals forces action.

Effect of R/C Molar Ratios and Dosages on MCX Adsorption

The structural characteristics of carbon xerogels could be affected by varying the molar ratio of resorcinol and catalyst (R/C), subsequently impacting the efficiency of pollutant removal by the carbon xerogels. Fig. 7 illustrated the removal of RB13 at different dosages of MCX with various R/C molar ratios.

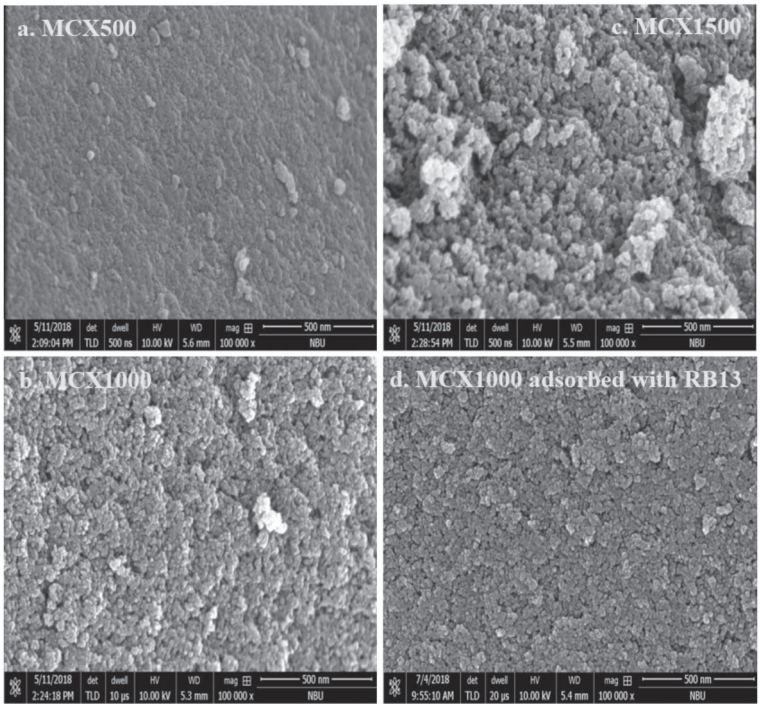

Fig. 5. SEM of some of the MCX samples.

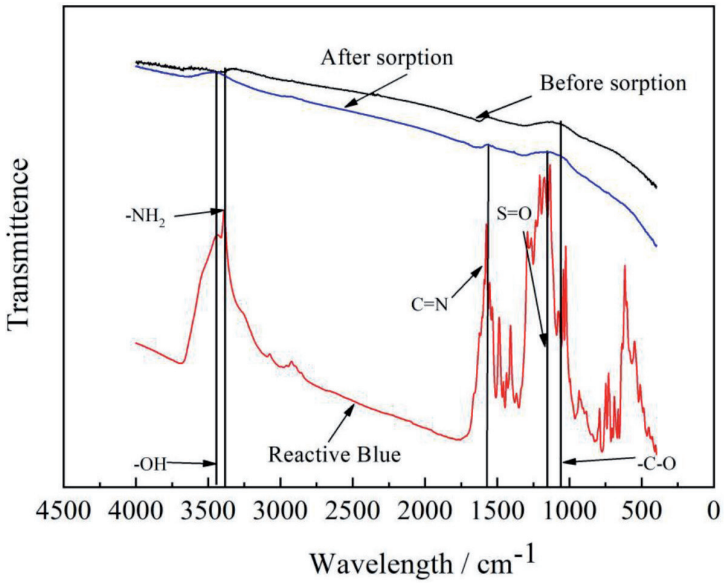

Fig. 6. FT-IR of MCX1000 before and after the sorption of RB13 dye.

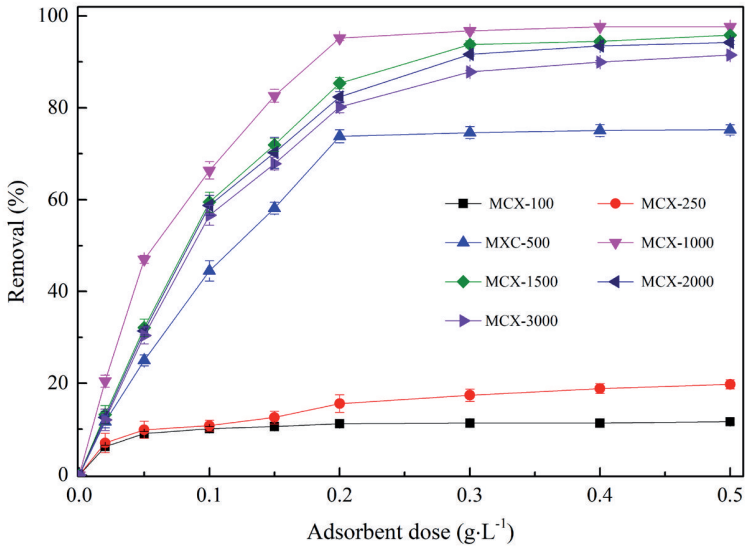

Fig. 7. Effect of different dosages of adsorbent on the removal of reactive blue 13 (initial concentration of RB13: 30 mg·L^{-1}; agitation speed: 180 rpm; temperature: 298 K; contact time: 12 h; adsorbent dose: 0.02~0.5 g·L^{-1}).

As the R/C molar ratio rose from 100 to 3000, there was an initial rise followed by a subsequent decline in the adsorption capacity of MCX for RB13.When the R/C molar ratio was less than 250, a limited quantity of dye molecules was adsorbed onto the surface of MCX due to the relatively lower specific surface area of MCX100 and MCX250. Subsequently, a sharp increment of RB13 removal as the R/C molar ratio further increased. The adsorbent MCX1000, synthesized at a R/C molar ratio of 1000 in the precursor mixture, exhibited the utmost adsorption capacity. As the R/C molar ratio exceeded 1500, the removal rate was gradually reduced, potentially attributable to the impact of the R/C molar ratio on the pore size, pore structure, and specific surface area of the carbon xerogels. When the molar ratio of R/C increased, the pore diameter became larger, the density decreased, and the specific surface area decreased (shown in Table 2 and Fig. 4), thereby polymer mesoporous carbon xerogels were formed, and otherwise colloidal granular mesoporous carbon xerogels were formed . Additionally, the R/C molar ratio exerted an influence on the pH of the prepared solution, thereby affecting the polycondensation of resorcinol and formaldehyde during the synthesis process

It was obvious that the removal of RB13 increased significantly initially and then increased slowly with the increment of adsorbent addition. When the dosage of adsorbent reached 0.2 g per liter of solution, the RB13 removal rate achieved a level exceeding 95% when utilizing MCX1000 as the adsorbent. This was mainly

because more total specific surface area and effective adsorption sites were supplied accompanied with more adsorbent addition, and then limited dye concentration restricted the continued increase of the removal rate. Consequently, for the subsequent adsorption experiments, MCX1000 was employed as the adsorbent at a dosage of 0.2 g per liter of solution.

Adsorption Kinetics

Adsorption kinetics is of great significance for designing adsorption systems. The augmentation of RB13 adsorption manifested a significant upsurge within the initial 50-minute contact duration, and then the adsorption gradually increased within the next 200 minutes in Fig. 8. After a contact time of 240 minutes, prolonging the duration of contact did not yield any enhancement in the adsorption effect. Initially, the adsorption rate exhibited rapidity owing to the adsorption of dye molecules on the external surface. Subsequently, the molecules permeated into the pores (internal surface), which constituted a comparatively sluggish process. The initial swiftness in the adsorption rate could be ascribed to the abundant presence of adsorption binding sites, whereas the eventual deceleration in the adsorption rate arose from site saturation and the achievement of equilibrium.

In order to comprehend the kinetics of the adsorption process, specifically with regard to the rate constant order, and determine the suitable mechanism explanation for adsorption along with the potential rate-controlling step, the pseudo-first-order, pseudo-second-order, intraparticle diffusion and Elovich models were tested for the adsorption of RB13 onto MCX1000 (Fig. 8). The best fit model was chosen based on nonlinear regression correlation coefficients R^2 values. All kinetic parameters obtained from fitting model plots with experimental data are presented in Table 3. It became apparent that the adsorption process closely conforms to the pseudo-second-order model, suggesting that chemical action primarily governs the adsorption process. This is consistent with the results of the study of negative dyes by Meriem [34]. Combined with FT-IR analysis, it can be inferred that hydrogen bonds dominate the RB13 adsorption process on both the inner and outer surfaces of MCX. The intraparticle diffusion curve does not originate from the origin, suggesting that intraparticle diffusion alone does not control the adsorption process entirely. The adherence of the adsorption efficiency to the Elovich model, as indicated by R^2, implied the presence of chemical effects, including hydrogen bonds, between RB13 and MCX during the heterogeneous adsorption process [35].

Adsorption Equilibrium Isotherms

The adsorption isotherm is a curve that describes the adsorption equilibrium between an adsorbent and an adsorbate, revealing the fundamental characteristics and mechanisms of the adsorption process through its shape, adsorption capacity, and equilibrium properties. It can be interpreted from Fig. 9 that the adsorption of RB13 on MCX increased as the initial concentration increased. However, equilibrium is reached once the saturation point is achieved, meaning that all effective adsorption sites on MCX have become saturated. As presented in Table 4, the maximum equilibrium adsorption capacity could reach up to 184.36 $mg \cdot g^{-1}$.

From Fig. 9, it could be observed that the three models, namely Temkin, Koble-Corrigan, and Redlich-Peterson exhibit excellent fitting. The R^2 values exceed 0.95, and as temperature increases, they further exceed

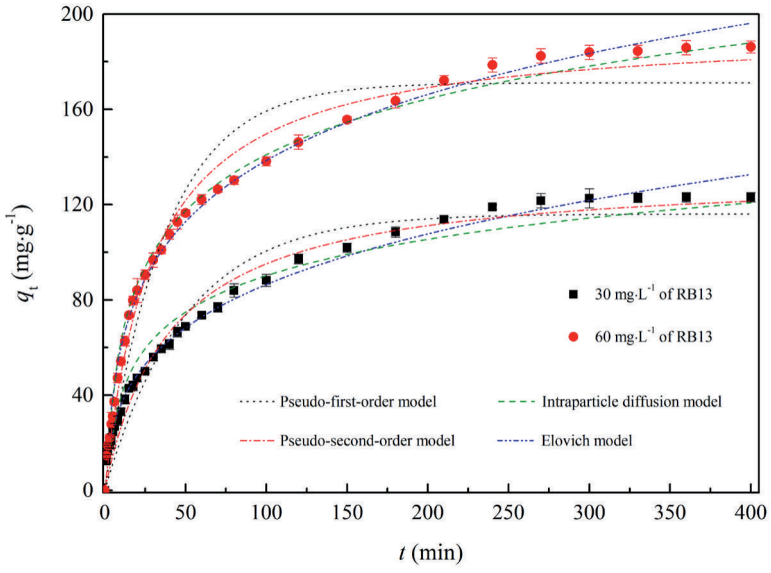

Fig. 8. Adsorption kinetics of RB13 onto MCX1000 and the kinetic models fitting (adsorbent dosage: 0.2 $g \cdot L^{-1}$; initial concentration of RB13: 30 and 60 $mg \cdot L^{-1}$; agitation speed: 180 rpm; temperature: 298 K; time: 0~400 min).

Table 3. Fitting parameter values of kinetic models for adsorption process of MCX1000 to RB13.

Kinetic model	Constants	Initial concentration of RB13	
		30 mg·L^{-1}	60 mg·L^{-1}
Pseudo first-order	k_1 (min^{-1})	0.0201	0.0268
	q_e (mg·g^{-1})	116.06	171.13
	R^2	0.9454	0.9533
Pseudo second-order	k_2 (g·mg^{-1}·min^{-1})	1.84×10^{-4}	1.72×10^{-4}
	q_e (mg·g^{-1})	133.69	194.31
	R^2	0.9759	0.9876
Intra-particle diffusion	K_{int} (mg·g^{-1}·min$^{-1/2}$)	6.4229	9.5560
	C	15.259	28.289
	R^2	0.9894	0.9915
Elovich equation	α (mg·g^{-1}·min^{-1})	6.1941	12.6928
	β (g·mg^{-1})	0.0348	0.0249
	R^2	0.9927	0.9958
	$q_{e,exp}$ (mg·g^{-1})	123.2	185.3

Table 4. Fitting data of different isothermal adsorption models for adsorption process of MCX1000 to RB13.

Isotherm model	Constants	Temperature		
		298 K	308 K	318 K
Freundlich	K_F (mg$^{1-1/n}$ ·L$^{1/n}$· g^{-1})	106.90	92.62	82.97
	n (g·L^{-1})	6.075	5.565	5.893
	R^2	0.9373	0.9671	0.9764
Langmuir	q_{max} (mg·g^{-1})	184.36	178.07	154.91
	K_L (g·L^{-1})	4.092	1.099	1.245
	R^2	0.8435	0.8424	0.8475
Temkin	B_T (J·mol^{-1})	116.0	120.19	142.58
	K_T (L·mg^{-1})	222.65	106.05	106.41
	R^2	0.9621	0.9791	0.9965
Dubinin-Radushkevich	q_{max} (mg·g^{-1})	179.1	169.85	150.6
	β (mol^2·J^{-2})	3.17×10^{-8}	1.92×10^{-7}	2.60×10^{-7}
	E (kJ·mol^{-1})	3.969	1.613	1.386
	R^2	0.7862	0.6903	0.6379
Redlich-Peterson	K_R (L·g^{-1})	2.44×10^3	2.12×10^3	1.26×10^3
	α_R (L·mg^{-1})	19.72	20.78	13.38
	g	0.877	0.8472	0.8638
	R^2	0.9520	0.9738	0.9934
Koble-Corrigan	a_k (L·g^{-1})	180.65	142.19	132.89
	b_k (L·mg^{-1})	0.6913	0.518	0.5884
	n	0.3407	0.3502	0.359
	R^2	0.9565	0.9836	0.9977

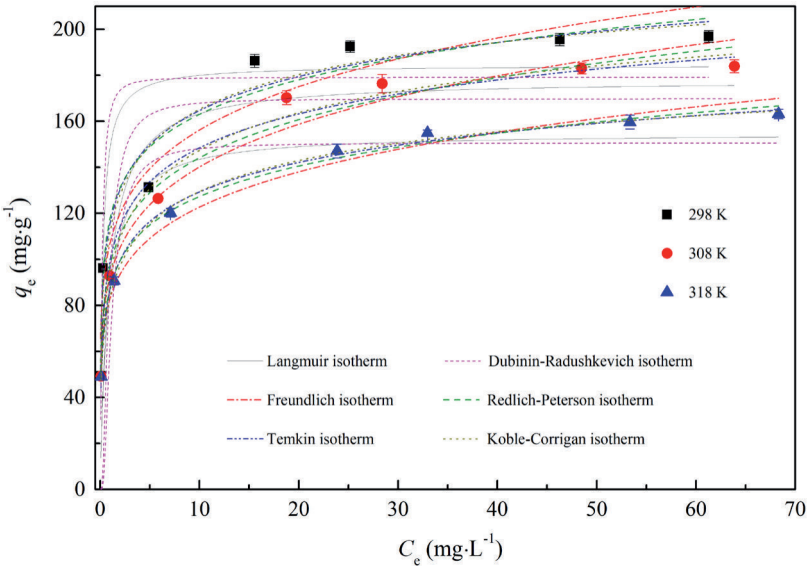

Fig. 9. Adsorption isotherm of RB13 onto MCX1000 and the isotherm models fitting under different temperatures (adsorbent dosage: 0.2 g·L^{-1}; initial concentration of RB13: 10~100 mg·L^{-1}; agitation speed: 200 rpm; contact time: 12 h; temperature: 298~318 K).

Table 5. Thermodynamic Fitting Parameters of MCX1000.

T (K)	K_c	ΔG° (KJ·mol^{-1})	ΔS° (J·(mol·K)$^{-1}$)	ΔH° (KJ·mol^{-1})	R^2
298	0.45	-2.64	-150.91	-47.61	0.99
308	0.25	-1.13			
318	0.08	-0.38			

0.99. The Temkin isotherm demonstrated the occurrence of physical adsorption. During the adsorption process, electrostatic interactions between the MCX surface and RB13, along with non-chemical interactions such as van der Waals forces, manifested their influence. Furthermore, within the temperature range of 298 to 318 K, the upward trend observed in the equilibrium binding constant (B) of the Temkin model as the temperature decreases highlights the unfavorable nature of higher temperatures for the uptake of dye molecules [36]. On the other hand, the Koble-Corrigan adsorption model proved suitable for chemical adsorption, revealing that adsorption predominantly proceeds through chemical reactions involving chemical bonds and surface-active sites [37]. The Redlich-Peterson adsorption model proved to be apt for the hybrid physical and chemical adsorption. In this model, due consideration was given to the impact of non-uniformity and distribution in the number of adsorption sites. Within the Redlich-Peterson framework, physical adsorption operated predominantly through non-chemical interactions, such as van der Waals forces and electrostatic interactions. On the other hand, chemical adsorption ensues via chemical reactions facilitated by chemical bonds and surface-active sites [38, 39]. Hence, the adsorption consonant with the Redlich-Peterson adsorption model manifests dual characteristics of physical and chemical adsorption, thereby functioning synergistically through these two mechanisms. This assertion aligned harmoniously with the findings obtained from FT-IR. Consequently, it could be deduced that the adsorption of RB13 onto MCX was attributed to physicochemical adsorption.

Adsorption Thermodynamics

The investigation of adsorption thermodynamics enables us to acquire a profound comprehension of the interconnectedness and alterations in energy that transpire throughout the adsorption process, thereby elucidating the mechanisms underlying adsorption and the disposition of adsorbate species on the surface of adsorbents.

The thermodynamic fitting of the data was conducted based on the prescribed formula, and the resultant outcomes were presented in Table 5. The value of the standard enthalpy of the reaction (ΔH°) implied that the RB13 adsorption was an exothermic process, so reducing the temperature facilitates the adsorption of the carbon gel to the RB13 adsorption, whereas the negative values of free enthalpy of sorption (ΔG°) indicate that the process was spontaneous [9, 38, 40].

Conclusions

This study demonstrates that mesoporous carbon xerogel presents itself as a promising adsorbent for RB13 removal. The findings reveal that the adsorption effect reaches its zenith when the molar ratio of resorcinol to sodium carbonate is at 1000:1 (MCX1000), and the optimal dosage is 200 $mg \cdot L^{-1}$, with an adsorption equilibrium time of 180 minutes. The maximum equilibrium adsorption amount attained is 184.36 $mg \cdot g^{-1}$. By means of FT-IR and SEM, the adsorption of nitrogen-containing ions or nitrogen-containing functional groups on RB13 via hydroxyl and carboxyl groups on the mesoporous carbon dry gel surface was validated. Moreover, electrostatic interactions, hydrogen bonding, and van der Waals forces were identified between the aforementioned nitrogen-containing species on RB13 and hydroxyl and carboxyl groups on the gel surface. The adsorption kinetics adhered to a pseudo-second-order model while the equilibrium adsorption process was modeled utilizing Temkin, Koble-Corrigan, and Redlich-Peterson models. Adsorption thermodynamics confirm that the adsorption was spontaneous, exothermic, and physicochemical.

Acknowledgment

The authors would like to acknowledge financial support for this work provided by NSFC of China (No. 21507065) and Ningbo Municipal Public Welfare Science and Technology Plan Project (2022S119).

Conflict of Interest

There are no conflicts to declare.

References

1. YAO M., ZHANG X., LEI L. Removal of Reactive Blue 13 from Dyeing Wastewater by Self-Assembled Organobentonite in a One-Step Process. Journal of Chemical & Engineering Data, **57** (7), 1915, **2012**.
2. NASEERUTEEN F., HAMID N.S.A., SUAH F.B.M., NGAH W.S.W., MEHAMOD F.S. Adsorption of malachite green from aqueous solution by using novel chitosan ionic liquid beads. International Journal of Biological Macromolecules, **107**, 1270, **2018**.
3. ZHANG Z., ZHANG M., ZHAO X., CAO J. High-efficient removal and adsorption mechanism of organic dyes in wastewater by KOH-activated biochar from phenol-formaldehyde resin modified wood. Separation and Purification Technology, **330**, **2024**.
4. LAHRECHE S., MOULEFERA I., EL KEBIR A., SABANTINA L., KAID M. H., BENYOUCEF A. Application of Activated Carbon Adsorbents Prepared from Prickly Pear Fruit Seeds and a Conductive Polymer Matrix to Remove Congo Red from Aqueous Solutions. Fibers, **10** (1), **2022**.
5. HIEN N.T., NGUYEN L.H., TAP VAN H., NGUYEN T.D., NGUYEN T.H.V., CHU T.H.H., NGUYEN T.V., TRINH V.T., VU X.H., AZIZ K.H.H,. Heterogeneous catalyst ozonation of Direct Black 22 from aqueous solution in the presence of metal slags originating from industrial solid wastes. Separation and Purification Technology, **233**, 115961, **2020**.
6. AWASTHI A., DATTA D. Application of Amberlite XAD-7HP resin impregnated with Aliquat 336 for the removal of Reactive Blue 13 dye: Batch and fixed-bed column studies. Journal of Environmental Chemical Engineering, **7** (6), **2019**.
7. BENKHAYA S., M'RABET S., EL HARFI A. Classifications, properties, recent synthesis and applications of azo dyes. Heliyon, **6** (1), **2020**.
8. AWASTHI A., ARYA A., GUPTA P., KUMAR R., SINGH J., DATTA D. Adsorption of Reactive Blue-13, an Acidic Dye, from Aqueous Solution Using Magnetized Activated Carbon. Journal of Chemical & Engineering Data, **65** (4), 2220, **2020**.
9. SIRAJUDHEEN P., KARTHIKEYAN P., VIGNESHWARAN S., MEENAKSHI S. Complex interior and surface modified alginate reinforced reduced graphene oxide-hydroxyapatite hybrids: Removal of toxic azo dyes from the aqueous solution. International Journal of Biological Macromolecules, **175**, 361, **2021**.
10. BENKHAYA S., ACHIOU B., OUAMMOU M., BENNAZHA J., ALAMI YOUNSSI S., MRABET S., EL HARFI A. Preparation of low-cost composite membrane made of polysulfone/polyetherimide ultrafiltration layer and ceramic pozzolan support for dyes removal. Materials Today Communications, **19**, 212, **2019**.
11. DEMISSIE H., AN G., JIAO R., RITIGALA T., LU S., WANG D. Modification of high content nanocluster-based coagulation for rapid removal of dye from water and the mechanism. Separation and Purification Technology, **259**, **2021**.
12. JOSEPH J., RADHAKRISHNAN R.C., JOHNSON J.K., JOY S.P., THOMAS J. Ion-exchange mediated removal of cationic dye-stuffs from water using ammonium phosphomolybdate. Materials Chemistry and Physics, **242**, **2020**.
13. ISMAIL G.A., SAKAI H. Review on effect of different type of dyes on advanced oxidation processes (AOPs) for textile color removal. Chemosphere, **291**, **2022**.
14. VARJANI S., RAKHOLIYA P., NG H.Y., YOU S., TEIXEIRA J.A. Microbial degradation of dyes: An overview. Bioresource Technology, **314**, **2020**.
15. HAO S., ZHANG T., FAN S., JIA Z., YANG Y. Preparation of COF-TpPa1 membranes by chemical vapor deposition method for separation of dyes. Chemical Engineering Journal, **421**, **2021**.
16. JIANG L., LU X.-Y., GENG Y.-Z., JIA Z.-Q., AN Q.-F., BRUGGEN B.V. Facile preparation of Porous aromatic frameworks PAF-56 membranes for nanofiltration of dyes solutions. Separation and Purification Technology, **280**, **2022**.
17. PAL P., CORPUZ A.G., HASAN S.W., SILLANPÄÄ M., BANAT F. Simultaneous removal of single and mixed cationic/anionic dyes from aqueous solutions using flotation by colloidal gas aphrons. Separation and Purification Technology, **255**, **2021**.
18. YAN Y., ZHOU P., ZHANG S., YIN X., ZENG X., PI P., NONG Y., WEN X. Facile preparation of ultralong polypyrrole nanowires-coated membrane for switchable

emulsions separation and dyes adsorption. Journal of Water Process Engineering, **49**, **2022**.
19. FÉLIX A.F.J.L. Organic Dyes versus Adsorption Processing. Molecules, **26** (18), 5440, **2021**.
20. GARCÍA-GONZÁLEZ A., ZAVALA-ARCE R.E., AVILA-PÉREZ P., RANGEL-VAZQUEZ N.A., SALAZAR-RÁBAGO J.J., GARCÍA-RIVAS J. L., GARCÍA-GAITÁN B. Experimental and theoretical study of dyes adsorption process on chitosan-based cryogel. International Journal of Biological Macromolecules, **169**, 75, **2021**.
21. PATON-CARRERO A., SANCHEZ P., SÁNCHEZ-SILVA L., ROMERO A. Graphene-based materials behaviour for dyes adsorption. Materials Today Communications, **30**, **2022**.
22. YAO T., QIAO L., DU K. High tough and highly porous graphene/carbon nanotubes hybrid beads enhanced by carbonized polyacrylonitrile for efficient dyes adsorption. Microporous and Mesoporous Materials, **292**, **2020**.
23. OSAGIE C., OTHMANI A., GHOSH S., MALLOUM A., KASHITARASH ESFAHANI Z., AHMADI S. Dyes adsorption from aqueous media through the nanotechnology: A review. Journal of Materials Research and Technology, **14**, 2195, **2021**.
24. MARCINIAK M., GOŚCIAŃSKA J., NORMAN M., JESIONOWSKI T., BAZAN-WOŹNIAK A., PIETRZAK R. Equilibrium, Kinetic, and Thermodynamic Studies on Adsorption of Rhodamine B from Aqueous Solutions Using Oxidized Mesoporous Carbons. Materials, **15** (16), 5573, **2022**.
25. PEKALA R.W. Organic aerogels from the polycondensation of resorcinol with formaldehyde. Journal Of Materials Science, **24**, 3221, **1989**.
26. VESELOV G., VEDYAGIN A. Resorcinol–Formaldehyde-Derived Carbon Xerogels: Preparation, Functionalization, and Application Aspects. Materials, **16** (19), **2023**.
27. ÁLVAREZ-MANUEL L., ALEGRE C., SEBASTIÁN D., EIZAGUERRI A., NAPAL P.F., LÁZARO M.J. N-doped carbon xerogels from urea-resorcinol-formaldehyde as carbon matrix for Fe-N-C catalysts for oxygen reduction in fuel cells. Catalysis Today, **418**, **2023**.
28. PTASZKOWSKA-KONIARZ M., GOSCIANSKA J., BAZAN-WOZNIAK A., PIETRZAK R. Amine-Modified Carbon Xerogels as Effective Carbon-Based Adsorbents of Anionic Dye from Aqueous Solutions. Materials, **15** (16), **2022**.
29. ZHAO B., ZHAO Y., LIU P., MEN Y.-L., PAN Y.-X. Boosting the adsorption and removal of dye from water by COOH-functionalized carbon nanotubes. Green Chemical Engineering, **4** (1), 88, **2023**
30. PTASZKOWSKA-KONIARZ M., GOSCIANSKA J., PIETRZAK R. Removal of rhodamine B from water by modified carbon xerogels. Colloids and Surfaces A: Physicochemical and Engineering Aspects, **543**, 109, **2018**.
31. SRIRAM G., BHAT M.P., KIGGA M., UTHAPPA U.T., JUNG H.-Y., KUMERIA T., KURKURI M.D. Amine activated diatom xerogel hybrid material for efficient removal of hazardous dye. Materials Chemistry and Physics, **235**, **2019**.
32. SUDAN S., KHAJURIA A., KAUSHAL J. Adsorption potential of pristine biochar synthesized from rice husk waste for the removal of Eriochrome black azo dye. Materials Today: Proceedings, **2023**.
33. CANAL-RODRÍGUEZ M., REY-RAAP N., MENÉNDEZ J.Á., MONTES-MORÁN M.A., FIGUEIREDO J.L., PEREIRA M.F.R., ARENILLAS A. Effect of porous structure on doping and the catalytic performance of carbon xerogels towards the oxygen reduction reaction. Microporous and Mesoporous Materials, **293**, **2020**.
34. KASBAJI M., MENNANI M., GRIMI N., OUBENALI M., MBARKI M., EL ZAKHEM H., MOUBARIK A. Adsorption of cationic and anionic dyes onto coffee grounds cellulose/sodium alginate double-network hydrogel beads: Isotherm analysis and recyclability performance. International Journal of Biological Macromolecules, **239**, 124288, **2023**.
35. SHOUMAN M.A., FATHY N.A. Microporous nanohybrids of carbon xerogels and multi-walled carbon nanotubes for removal of rhodamine B dye. Journal of Water Process Engineering, **23**, 165, **2018**.
36. ADEDEJI O.M., JAHAN K. Removal of pollutants from aqueous product of Co-hydrothermal liquefaction: Adsorption and isotherm studies. Chemosphere, **321**, 138165, **2023**.
37. MPATANI F.M., ARYEE A.A., KANI A.N., WEN K., DOVI E., QU L., LI Z., HAN R. Removal of methylene blue from aqueous medium by citrate modified bagasse: Kinetic, Equilibrium and Thermodynamic study. Bioresource Technology Reports, **11**, **2020**.
38. LAWTAE P., TANGSATHITKULCHAI C. The Use of High Surface Area Mesoporous-Activated Carbon from Longan Seed Biomass for Increasing Capacity and Kinetics of Methylene Blue Adsorption from Aqueous Solution. Molecules, **26** (21), **2021**.
39. NAKHJIRI M.T., MARANDI G.B., KURDTABAR M. Poly(AA-co-VPA) hydrogel cross-linked with N-maleyl chitosan as dye adsorbent: Isotherms, kinetics and thermodynamic investigation. International Journal of Biological Macromolecules, **117**, 152, **2018**.
40. MEN J., SHI H., DONG C., YANG Y., HAN Y., WANG R., ZHANG Y., ZHAO T., LI J. Preparation of poly(sodium 4-styrene sulfonate) grafted magnetic chitosan microspheres for adsorption of cationic dyes. International Journal of Biological Macromolecules, **181**, 810, **2021**.
41. KIM Y.-S., KIM J.-H. Isotherm, kinetic and thermodynamic studies on the adsorption of paclitaxel onto Sylopute. The Journal of Chemical Thermodynamics, **130**, 104, **2019**.
42. LIM Y.-S., KIM J.-H. Isotherm, kinetic and thermodynamic studies on the adsorption of 13-dehydroxybaccatin III from Taxus chinensis onto Sylopute. The Journal of Chemical Thermodynamics, **115**, 261, **2017**.
43. WU F.-C., TSENG R.-L., JUANG R.-S. Characteristics of Elovich equation used for the analysis of adsorption kinetics in dye-chitosan systems. Chemical Engineering Journal, **150** (2-3), 366, **2009**.
44. DEBORD J., HAREL M., BOLLINGER J.-C., CHU K. H. The Elovich isotherm equation: Back to the roots and new developments. Chemical Engineering Science, **262**, **2022**.
45. GEIES A., GOMAA G.S., IBRAHIM S.M., AL-HOSSAINY A.F., ABDELWADOUD F.K. Experimental and simulated TD-DFT study of malachite green dye and tetrahydroquinoxaline hybrid blend: Its application removal from wastewater. Journal of Molecular Structure, **1291**, **2023**.
46. CALVETE T., LIMA E.C., CARDOSO N.F., VAGHETTI J.C.P., DIAS S.L.P., PAVAN F.A. Application of carbon adsorbents prepared from Brazilian-pine fruit shell for the removal of reactive orange 16 from aqueous solution: Kinetic, equilibrium, and thermodynamic studies. Journal of Environmental Management, **91** (8), 1695, **2010**.

47. ALI F., ALI N., BIBI I., SAID A., NAWAZ S., ALI Z., SALMAN S.M., IQBAL H.M.N., BILAL M. Adsorption isotherm, kinetics and thermodynamic of acid blue and basic blue dyes onto activated charcoal. Case Studies in Chemical and Environmental Engineering, **2**, **2020**.

48. AÇIKYILDIZ M., GÜRSES A., GÜNEŞ K., YALVAÇ D. A comparative examination of the adsorption mechanism of an anionic textile dye (RBY 3GL) onto the powdered activated carbon (PAC) using various the isotherm models and kinetics equations with linear and non-linear methods. Applied Surface Science, **354**, 279, **2015**.